Applied Catalysis B: Environmental 339 (2023) 123160

Contents lists available at ScienceDirect

Applied Catalysis B: Environmental

journal homepage: www.elsevier.com/locate/apcatb

Design principles for selective and economical CO_2 electrolysis in acids

Jaehoon Kim [a,1], Tae Hyeon Ha [a,1], Junehyeok Kim [b,1], Gyoung Hwa Jeong [a,c], Sang Ouk Kim [a,c], Wonsuk Chung [b], Kosan Roh [d,*], Jay H. Lee [b,e,**], Jihun Oh [a,*]

[a] Department of Materials Science and Engineering, Korea Advanced Institute of Science and Technology (KAIST), 291 Daehak-ro, Yuseong-gu, Daejeon 34141, Republic of Korea
[b] Department of Chemical and Biomolecular Engineering, KAIST, 291 Daehak-ro, Yuseong-gu, Daejeon 34141, Republic of Korea
[c] National Creative Research Initiative (CRI) Center for Multi-Dimensional Directed Nanoscale, KAIST, 291 Daehak-ro, Yuseong-gu, Daejeon 34141, Republic of Korea
[d] Department of Chemical Engineering and Applied Chemistry, Chungnam National University, 99 Daehak-ro, Yuseong-gu, Daejeon 34134, Republic of Korea
[e] Mork Family Department of Chemical Engineering and Materials Science, University of Southern California, 3651 Watt Way, Los Angeles, CA 90089, United States

ARTICLE INFO

Keywords:
Electrochemical CO_2 reduction
Flow cell
Acid electrolyte
Ni single-atom catalyst
Techno-economic and Life cycle assessment

ABSTRACT

The electrochemical CO_2 reduction reaction (CO_2RR) is a promising pathway for converting CO_2 into valuable products such as carbon monoxide (CO). Here we show that a remarkably high CO selectivity can be achieved in a gas diffusion electrode-based CO_2RR flow cell by using different characteristics of the proton and CO_2 reduction reactions over a wide range of pHs, while H_2 evolution from H_2O reduction can be effectively avoided. The potential window of a high-performance Ni single-atom catalyst for CO_2RR does not overlap with that for H_2O reduction; this allows CO selectivity to exceed 90% in a pH 2 electrolyte, thereby attaining a CO_2-to-CO conversion rate of approximately 77%. Effects of electrolyte compositions on CO_2RR are also evaluated. Techno-economic and life cycle assessments establish that CO_2RR is more favorable in acidic conditions, which can minimize the additional CO_2 recycling and electrolyte regeneration processes, if surplus or cheap renewable electricity is available.

1. Introduction

The electrochemical CO_2 reduction reaction (CO_2RR), an electrified process that produces carbon-neutral fuels and value-added chemical feedstocks, has drawn intense interest as a viable technology for mitigating anthropogenic carbon emissions [1,2]. Carbon monoxide (CO) is an attractive CO_2RR product as it is a key component of syngas that can provide various hydrocarbons through the Fischer–Tropsch process [3–6]. To establish an economically beneficial electrochemical CO_2RR to CO process with negative carbon emissions compared to those generated during conventional fossil fuel-based CO production processes, efficient and selective CO_2 electrolysis at high current densities (i.e., ≥ -100 mA cm^{-2}) is required with high CO_2 single-pass conversion (SPC; the ratio of converted CO_2 to supplied CO_2) [7,8].

A gas-fed CO_2 electrolyzer with a catalyst-coated gas diffusion electrode (GDE) can electrocatalyze CO_2 to CO with high Faraday efficiency (FE) under industry-relevant current density [9,10]. Gas-fed CO_2 electrolyzers are typically operated in alkaline electrolytes for achieving a high energy efficiency and selectivity [11–14]. Unfortunately, the CO_2RR in alkaline electrolytes is accompanied by the following inevitable problems arising from the chemical reaction of CO_2 with the electrolyte to form carbonate ions (CO_3^{2-}): (1) carbonate salts gradually precipitate at or near GDEs and degrade electrode stability and efficiency [12,14–16]; (2) CO_3^{2-} decreases the ionic conductivity of the electrolyte/anion exchange membrane and thereby limits the energy efficiency of the CO_2 electrolyzer [15,17–19]; and most importantly, (3) SPC in alkaline electrolytes is theoretically limited to less than 50% as the fed CO_2 reacts with OH^- to form CO_3^{2-} [17–20]. This low SPC results in high carbon costs for the downstream product separation and CO_2 recovery process [18,21,22].

CO_2 electrolysis in an acid electrolyte offers promises to circumvent the pitfalls from the carbonate formation as carbonate and bicarbonate ions do not form in acid [18,20,22,23]. However, poor CO selectivity is anticipated to arise from the hydrogen evolution reaction (HER) in

* Corresponding authors.
** Corresponding author at: Mork Family Department of Chemical Engineering and Materials Science, University of Southern California, 3651 Watt Way, Los Angeles, CA 90089, United States.
E-mail addresses: ksroh@cnu.ac.kr (K. Roh), jlee4140@usc.edu (J.H. Lee), jihun.oh@kaist.ac.kr (J. Oh).
[1] These authors contributed equally to this work.

https://doi.org/10.1016/j.apcatb.2023.123160
Received 13 April 2023; Received in revised form 31 July 2023; Accepted 8 August 2023
Available online 9 August 2023

proton (H^+)-abundant acids. Recently, a few studies have demonstrated that the HER can be suppressed by controlling the local environment at/near electrodes during CO_2RR in acid [18,22,24,25]. For example, Bondue et al. demonstrated that local alkalinity at/near an Au electrode can neutralize H^+ and suppress the HER on the Au electrode under mildly acidic conditions (pH 3–4) [25]. More recently, Ni single atom catalysts are shown to be CO-selective even in stronger acidic electrolytes (< pH 2) [26,27]. In addition, the introduction of weakly hydrated cations (e.g., Cs^+) [24,27] or a high alkali cation concentration [22,26] in an electrolyte allows the use of more acidic electrolytes. Despite these encouraging results, however, CO selectivity is still limited to less than 80% even at high current densities [22,24]. To achieve a highly selective and economically meaningful CO_2RR, understanding how the intrinsic properties of a catalyst as well as the electrolysis environment influence the CO_2RR mechanisms under industry-relevant current densities is important.

In this work, we suggest design principles for selective CO production at high current densities in acid electrolytes based on mass transfer of CO_2 and H^+ and interfacial electro-kinetics. Our theoretical and experimental study revealed that CO_2RR in a gas-fed flow cell is inherently CO selective over H_2 by the H^+ reduction reaction in acids, but it is the water (H_2O) reduction reaction that deteriorates the CO selectivity, which can be effectively minimized by using a catalyst with better intrinsic CO activity. Ni single-atom catalysts supported on carbon nanotubes (Ni-SAC-CNTs) were used as a model system for superior CO production performance [14]. The Ni-SAC-CNTs exhibited a CO FE of >90% at −100 mA cm^{-2} and pH 2.0. In addition, weakly hydrated cations in electrolytes can generate high CO selectivity in acids by promoting CO_2RR and suppressing HER electro-kinetics. Additionally, a systematic investigation of the carbon balance during CO_2 electrolysis indicated that highly selective CO formation from Ni-SAC-CNTs, which is accompanied by significantly reduced CO_3^{2-} formation, leads to the highest CO_2-to-CO SPC of approximately 77% without tuning the local reaction environments. We also conceptually designed electrochemical CO production processes by employing both acid and alkaline electrolytes and analyzed their economic viability and environmental impact throughout their life cycle. We verified that the economic and environmental superiorities between the two processes are significantly affected by technical (e.g., cell voltage and SPC) as well as non-technical (e.g., prices and global warming impact (GWI) of utility) parameters.

2. Experimental

2.1. Materials

All materials were purchased from a commercial supplier and used as received without further purification, unless otherwise noted. High purity CO_2 (>99.999%) and ultrahigh purity N_2 (>99.9999%) gases were used in all electrochemical tests. Water was purified using a Millipore Milli-Q system (18.2 MΩ·cm) and used to prepare all the solutions.

2.2. Synthesis of Ni single-atom catalysts on carbon nanotubes supports (Ni-SAC-CNTs)

First, 10 mg of carbon nanotubes (CNTs, multi-walled, >98% carbon basis, 6–13 nm × 2.5–20 μm (O.D. × L), Sigma-Aldrich) were dissolved in 100 ml of methanol (Extra Pure, >99.6 v/v%, OCI), and sequentially the solution was sonicated for 5 min in order to well disperse. Subsequently, 2 mmol of nickel nitrate hexahydrate ($Ni(NO_3)_2{\cdot}6\,H_2O$, ≥ 98.5%, Sigma-Aldrich) and 80 mmol of 2-methylimidizole (2-MeIm, 99%, Sigma-Aldrich) were poured into the CNT dispersion. After stirring with a magnet for 3.5 h, a green-colored solution was obtained, which was kept overnight in an oven at 65 °C. Afterwards, an olive-green precipitate was centrifuged, washed using ethanol (Extra Pure, 94 v/v %, OCI), and dried in an oven at 80 °C for 3 h. The resultant solids were crushed into powders and then heated to 800 °C at 10 °C min^{-1} under ambient Ar conditions. After reaching the target carbonization temperature, the mixture was maintained for 2 h and then cooled to room temperature.

2.3. Preparation of catalyst-coated gas diffusion electrodes (Catalyst/GDE)

The catalyst/GDE was prepared by drop-casting the prepared catalyst ink on the microporous layer (MPL) side of a carbon paper (SIGRACET® GDL-39BC, SGL Carbon). For Ni-SAC-CNTs catalyst ink preparation, 20 mg of the catalyst powders were dispersed in a mixture of 10 ml of N,N-Dimethylformamide (DMF, ACS Reagent, >99.8%, Alfa Aesar) and 125 μl of Nafion 117 solution (5 wt%, Sigma-Aldrich). The as-prepared catalyst ink was sonicated for an hour to ensure a good mixing. The well-dispersed ink was then drop-casted onto carbon paper placed on a hot plate, which was kept at 150 °C until the loading mass per unit area reached to about 0.8 mg cm_{geo}^{-2}. For the preparation of Ag nanopowders coated on a GDE (Ag NPs/GDE), all procedures were the same as those described above, but the catalyst powders were based on commercial Ag nanopowders (Ag NPs, Avg. size <150 nm, 99%, Sigma-Aldrich) and isopropyl alcohol (IPA, Electronic Grade, >99.9%; Chemitop) were used as the dispersion solvents instead of DMF.

Meanwhile, for understanding the effect of electrolyte cations and anions on the CO_2RR and HER in acids, Ag/GDE was used as a model catalyst and prepared as follows: a 130 nm-thick Ag thin film was deposited at a rate of 2.5 Å s^{-1} on the MPL side of the carbon paper (SIGRACET® GDL-39BC) with an e-beam evaporator (e-VapTM, I.T.S).

2.4. Configuration of gas-fed flow cells with catalyst-coated GDEs

A lab-made gas-fed flow cell was used for all electrochemical measurements. The flow cell was composed of anode and cathode chambers separated by ion-exchange membranes. Different ion-exchange membranes were applied to the flow cell depending on the electrolyte pH: Nafion™ membrane (NRE-212, Alfa Aesar) was used as the acid electrolyte, while Selemion™ (AMVN, AGC Engineering) and Sustainion® (X37–50 Grade RT, Dioxide Materials) membranes were used for near-neutral (pH 8.3) and alkaline (pH 14.0) electrolytes, respectively. Ag/AgCl (saturated KCl, RE-1B, EC-Frontier) was used as the reference electrode. The prepared catalyst/GDE whose catalyst loading was 0.8 mg cm_{geo}^{-2} (approximately 0.1 mg cm_{geo}^{-2} for the Ag/GDE) was used as a working electrode, and iridium oxide electrode (IrO_2/carbon paper, Dioxide Materials) for acids and a commercial NiFeCuMo foil (0.125 mm-thick, Mumetal®, Alfa Aesar) for pH> 8 electrolytes were used as counter electrodes, respectively. Note that the types of the anode do not affect the performance of the working electrode (i.e., cathode) in a 3-electrode measurement. The geometric area of both the electrodes exposed to the electrolyte was 2 cm^2. For each electrochemical test, an electrolyte was circulated in and out of the cathode compartment with a peristatic pump (MU-D01, Major Science) from a 100 ml electrolyte reservoir at a flow rate of ~14 ml min^{-1}. However, the same electrolyte was not circulated but just filled in the anode compartment (~8 ml), which has an opening for O_2 gas to escape.

2.5. Electrochemical measurements

All electrochemical measurements were performed using an electrochemical workstation (VSP Potentiostat, BioLogic) with electrochemical impedance spectroscopy (EIS) and a high-current booster (VMP3B-5, 5 A/20 V, BioLogic). Electrolytes with pH from 0.5 to 7.3 were prepared using phosphate buffer solutions based on combinations of phosphoric acid (H_3PO_4, ACS Reagent, ≥85 wt% in H_2O, Sigma-Aldrich) and/or potassium phosphate monobasic (KH_2PO_4, Extra Pure, >99%, Daejung Chemicals & Metals) and/or dibasic (K_2HPO_4, Extra Pure, >99%, Daejung Chemicals & Metals). The electrolytes with pH

8.3, and 14.0 were prepared using potassium bicarbonate ($KHCO_3$, ACS Reagent, 99.7%, Sigma-Aldrich), and potassium hydroxide (KOH, ACS Reagent, ≥85%, Sigma-Aldrich), respectively. The detailed concentrations used to determine the pH of interest are summarized in the table below.

pH[a]	Concentration (M)				
	H_3PO_4	KH_2PO_4	K_2HPO_4	$KHCO_3$	KOH
0.5	3.2	0.25			
1.0	1.4	0.25			
2.0	0.236	0.264			
3.2	0.032	0.468			
5.0		0.487	0.013		
6.0		0.378	0.122		
7.3		0.097	0.403		
8.3				1.0	
14.0					1.0

[a] Electrolyte pH values were measured using a digital pH meter (Orion Star™ A211, Thermo Scientific).

In addition, the effect of buffer capacity was evaluated in sulfate- and phosphate-based pH 2.0 electrolyte. The sulfate-based pH 2.0 electrolyte consists of 0.01 M sulfuric acid (H_2SO_4, Extra Pure, 95%, Daejung Chemicals & Metals) and 0.13 M potassium sulfate (K_2SO_4, ACS Reagent, ≥99.0%, Sigma-Aldrich), while the composition of pH 2.0 electrolyte with phosphate anion was the same as described in the table above. To investigate the effect of alkali cations, different alkali metal sulfates (M_2SO_4 where M = Li, K, and Cs) were added in the non-buffer pH 2.0 electrolyte: 0.01 M H_2SO_4 + 0.13 M $Li_2SO_4{\cdot}H_2O$ (ACS Reagent, ≥99.0%, Sigma-Aldrich), K_2SO_4 (ACS Reagent, ≥99.0%, Sigma-Aldrich), and Cs_2SO_4 (99.99%, Sigma-Aldrich), respectively.

In all electrochemical measurements, except for the LSV studies, chronopotentiometry was carried out for 20 min under various CO_2 flow rates of ≤ 20 sccm, controlled by a mass flow controller (VIC-D210; MFC Korea). Note that a pre-reduction step was conducted at −10 mA cm^{-2}_{geo} for 10 min before each electrochemical measurement [14]. During CO_2 electrolysis, the solution resistance was collected by the EIS at each experimental interval, and unless otherwise stated, the ohmic drop (iR) was 100% manually compensated by subtracting the solution resistance multiplied by the total current from the applied potential. The applied potentials (vs. Ag/AgCl, $E_{Ag/AgCl}$) of the working electrode were converted to the normal hydrogen electrode (NHE) scale (E_{NHE}) using the following equation:

$$E_{NHE}\ (V) = E_{Ag/AgCl}\ (V) - iR + 0.199\ V \quad (1)$$

LSV for identifying the characteristic profile of the H^+ and H_2O reduction reaction in pH 2.0 electrolyte with (or without) various alkali metal cations (e.g., Li^+, K^+, and Cs^+) and non-buffering anion (e.g., sulfate) was performed in the same gas-fed flow cell configurations. Under N_2 and CO_2 flowing with a nominal flow rate of 20 sccm, the potentials were scanned at a rate of 10 mV s^{-1} in cathodic direction from −0.3 V (vs. NHE).

The quantification of gas products from CO_2 electrolysis was carried out using an online gas chromatography (GC, 2-channel 3000 Micro GC, INFICON) equipped with a Plot Q column and a Molsieve 5 A column coupled with a thermal conductivity detector (TCD).

The formation rates per unit area ($\dot{n}$) for the gaseous products (CO and H_2) were calculated as follows:

$$\dot{n}_i \quad \left(nmol{\cdot}s^{-1}{\cdot}cm^{-2}_{geo}\right) = \frac{n_i}{A_{geo}{\cdot}t} \quad (2)$$

where n_i is the number of moles of the product (calculated from GC analysis) based on the outlet gas flow rate measured using an electronic flow meter (G6691A ADM flow meter, Agilent), A_{geo} is the geometric electrode area exposed to the electrolyte, and t is the operation time for CO_2 electrolysis. The Faraday efficiency (FE) of the products was calculated as follows:

$$FE_i \quad (\%) = \frac{n_i z_i F}{q} \quad (3)$$

where z_i is the stoichiometric number of electrons required to form the product (2 for CO and H_2), F is the Faraday constant (96485 C mol^{-1}), and q is the amount of charge passed during CO_2 electrolysis. The CO partial current density was calculated by multiplying the CO FE by the total applied current density.

For the stability test, CO_2 electrolysis was performed for 10 h at a constant −100 mA cm^{-2}_{geo} in a pH 2.0 electrolyte under a nominal CO_2 flow rate of 20 sccm. Online gas chromatography (GC) sampling to quantify the gas products was performed every 30 min. The electrolyte was neither supplemented nor exchanged by new one during the stability test.

The single-pass conversion was calculated as following equation:

$$Single-pass\ conversion\ (\%) = \frac{Q_{CO}}{Q_{CO_2,inlet}} \times 100(\%) \quad (4)$$

where Q_{CO} is the calculated CO flow rate obtained by multiplying the CO quantity measured at the GC by the outlet gas mixture flow rate measured at the outlet stream of the cathode chamber, and $Q_{CO2,inlet}$ is the CO_2 flow rate supplied to the cathode compartment.

2.6. Materials characterization

The morphology of Ni-SAC-CNTs/GDE before and after the 10 h stability test for CO_2 electrolysis was observed through field emission scanning electron microscopy with an acceleration voltage of 1.00 kV (FE-SEM; JSM-IT800; JEOL). Elemental mapping over the catalysts was conducted in a JSM-IT800 at 15.0 kV equipped with an energy dispersive X-ray spectrometer (EDS) system (QUANTAX EDS system, Bruker).

2.7. Major specifications of process design, TEA and LCA

CO_2RR processes with acid/alkaline electrolytes were conceptually designed in a MATLAB environment. The plant capacity of the designed processes were 150,000 tons/y, with 8000 annual operating hours. The target purity of the CO product was 97 wt%, which is suitable for phosgene production. The oxygen by-product from the anode side for both the acid and alkaline cases was assumed to be vented.

The mass balance of the electrolyzer was calculated using Faraday's law: An amine scrubbing unit with monoethanolamine (MEA) for CO_2 recovery from the cathodic effluent stream was designed using the commercial process simulator Aspen Plus®. The electrolyte non-random two-liquid (NRTL) model was applied for the thermodynamic calculations. Owing to the accumulation of CO_2 as carbonate in the alkaline electrolyte, a calcium caustic recovery loop was added for the separation of CO_2 from the electrolyte. The separated CO_2 and electrolyte were recycled to the cathode inlet and the electrolyzer, respectively. Utility usage of the calcium caustic recovery loop was obtained from Keith et al. [28].

In the TEA, the InSide Battery Limit (ISBL) and Outside Battery Limit (OSBL) approaches [29] were adopted for the annual capital expenditure (CAPEX) calculation. In the LCA, the cradle-to-gate system boundary was applied for calculating the carbon footprint. The TEA and LCA methodologies are described in *Note S4–2* and *S4–3*, respectively. The price and GWI values used for the South Korea/Norway scenario and the sensitivity analysis results are listed in Table S7 and S12. Inventory data calculation and the TEA/LCA results for the South Korean and Norwegian scenarios are shown in Table S8–S11.

3. Results and discussion

3.1. Equilibrium concentrations of CO_2 and H^+ in various pH solutions

The H_2O–CO_2 equilibrium diagram justifies the use of an acid electrolyte for the efficient utilization of CO_2 during the CO_2RR. Fig. 1a shows the solubility diagram of CO_2 as a function of pH for an ideal open CO_2–H_2O system (i.e., $T = 25$ °C; $P_{CO2} = 1.0$ atm; no salting in and out effects). This diagram was constructed based on the mass action law for all relevant species in the system (see details in *Note S1* of Supplementary Material). The total concentration of dissolved CO_2 ([total CO_2]) is the sum of three inorganic carbon species: carbonic acid (H_2CO_3), bicarbonate (HCO_3^-), and carbonate (CO_3^{2-}). H_2CO_3 is denoted as CO_2(aq) because the kinetics of the forward reaction ($CO_2(aq) + H_2O \leftrightarrow H_2CO_3$) is slow [30]. As shown in Fig. 1a, [total CO_2] dramatically increased when pH > pK_1 (= 6.35) in the form of HCO_3^- and CO_3^{2-}. Because HCO_3^- and CO_3^{2-} cannot be reduced electrochemically, this indicates that large amounts of the CO_2 fed will be wasted in a flow cell if neutral or alkaline electrolytes are used (Fig. S1). In contrast, nearly 100% of CO_2 in an electrolyte with pH < 6 will be available for electrochemical reduction to CO.

The H_2O–CO_2 equilibrium diagram also provides insights into the electrochemical activity of CO_2RR and HER by showing [CO_2(aq)] and [H^+] as a function of pH. For instance, [CO_2(aq)] is 33 mM at $T = 25$ °C and $P_{CO2} = 1.0$ atm and is independent of pH, whereas [H^+] = 10^{-pH} M. Interestingly, [CO_2(aq)] prevails over [H^+] in most electrolytes, except in strong acids (pH < 1.5). Since CO_2(aq) and H^+ are the reactants for CO_2RR and HER, respectively, it implies that CO_2RR could be inherently favored over HER in various electrolytes when both electrochemical rates are limited by the mass transport of [CO_2(aq)] and [H^+] at high overpotentials.

To further understand the electrode kinetics of CO_2RR and HER, we performed theoretical calculations using the Butler–Volmer equation modified with the mass transfer effect. Fig. 1b shows the calculated current density-potential (*j-V*) curves for CO_2-to-CO reduction and H^+ reduction reactions in a pH 2.0 solution (see the details of the theoretical calculation method in *Note S2*). In Fig. 1b, the electrochemical characteristics of a catalyst are represented with effective exchange current densities that include the effects of intrinsic catalytic properties (such as active sites) and the local environments (such as cation effect). The effective exchange current densities for the CO_2-to-CO ($j^{eff}_{0,CO2}$) and H^+ reduction reaction (j^{eff}_{0,H^+}) are set to 1 mA cm^{-2}, respectively. In Fig. 1b, we also consider the electrode kinetics in two different CO_2 electrolyzers: a conventional H- and a gas-fed flow cell. In an H-cell, CO_2 is supplied to an electrode from a bulk electrolyte and the CO_2RR kinetics is limited by the mass transfer of CO_2, which becomes potential-independent at high overpotentials. Meanwhile, in a gas-fed flow cell, CO_2 is supplied to an electrode through the backside of a GDE, and the fast diffusion of gas-phase CO_2 makes CO_2RR limited by the charge transfer at an electrode of which rate increases exponentially with

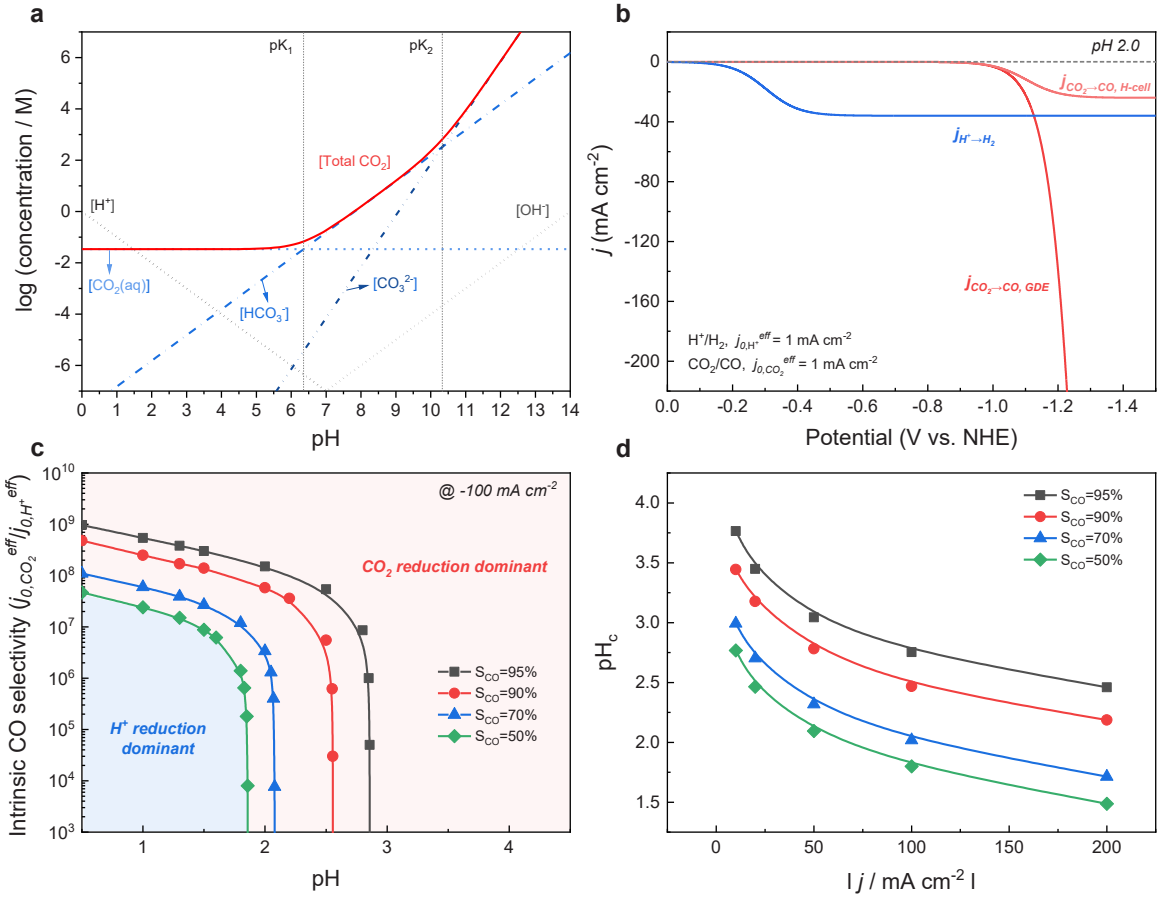

Fig. 1. Theoretical calculations for intrinsic CO selectivity as a function of pH in a gas-fed flow cell. (a) Plot of log concentration of inorganic carbon species (e.g., CO_2(aq); HCO_3^-; CO_3^{2-}), H^+ and OH^- as a function of pH for an open CO_2–H_2O system at $T = 25$ °C and $P_{CO2} = 1.0$ atm. (b) Calculated current density-potential (*j-V*) curves for CO_2-to-CO reaction and H^+ reduction reaction in a pH 2.0 solution in two different types of CO_2 electrolyzer (H- and gas-fed flow cell). It is noted that the same effective exchange current density was set as 1 mA cm^{-2} to CO_2-to-CO and H^+ reduction reactions, respectively. (c) Plot of calculated intrinsic CO selectivity as a function of pH with respect to various target CO selectivities (S_{CO}s) from 50% to 95% in a gas-fed flow cell. Note that the intrinsic CO selectivity is defined as the ratio of effective exchange current density of CO_2RR to that of HER ($j^{eff}_{0,CO2}/j^{eff}_{0,H^+}$). (d) Plot of critical pH (pH_c) as a function of current density for different target S_{CO}s in a gas-fed flow cell. The pH_c is defined as the minimum pH at which target CO selectivity would be achieved irrespective to an intrinsic CO selectivity of a catalyst.

overpotential [9,10]. In both cells, the HER was limited by the mass transfer of H^+ to the electrode from the bulk electrolyte.

The different nature of the electrode kinetics of CO_2 and H^+ reduction reactions in a gas-fed flow cell endows inherent CO selectivity at industry-relevant current densities in low-pH electrolytes. The charge-transfer-limited CO_2RR rate far exceeded the mass-transfer-limited H^+ reduction rate with increasing overpotential in various pH solutions. As shown in Fig. 1b, even a neutral catalyst is capable of producing CO with a selectivity of 82% at -200 mA cm^{-2} in a gas-fed flow cell, whereas HER is dominant at all potentials in an H-cell. Interestingly, the intrinsic property of a catalyst does not influence CO selectivity if the pH of the electrolyte is larger than the critical pH (pH_c), which is defined as the minimum pH required to achieve target CO selectivity irrespective of the intrinsic CO selectivity ($j^{eff}_{0,CO2}$ / j^{eff}_{0,H^+}) of the catalyst (Fig. 1c). For example, the CO production becomes dominant with > 90% CO selectivity at -100 mA cm^{-2} in an electrolyte with pH_c of 2.5, regardless of the intrinsic properties of the catalyst. Although it is necessary for a catalyst to have an intrinsic CO selectivity ($j^{eff}_{0,CO2}$ / j^{eff}_{0,H^+}) of over 10^7 for dominant CO production in a strong acid (pH < 1.5), pH_c decreases with increasing current density (Fig. 1c-d). Therefore, our theoretical calculation indicates that carrying out CO_2RR at a current density > –200 mA cm^{-2} enables CO production with selectivity > 95%, irrespective of the intrinsic properties of the catalyst in a mild acid (pH ~2.5) in a gas-fed flow cell.

3.2. Effect of pH on electrochemical CO_2RR and HER of Ni-SAC-CNTs and Ag NPs

Inspired by the insight from the theoretical calculation, we investigated the effect of electrolyte pH on CO_2RR and HER activity using electrocatalysts with different intrinsic properties in a gas-fed flow cell. In this work, we used Ni-SAC-CNTs/GDE and commercial Ag NPs/GDE as a model catalyst system (see more details of preparation in *Experimental* Section). Ni-SAC-CNTs/GDE represents an electrocatalyst with superior intrinsic activity compared to that of commercial Ag NPs/GDE. Indeed, Ni-SAC-CNTs/GDE activates CO production at an onset potential approximately 0.3 V lower than that of Ag NPs/GDE in alkaline, near-neutral, and acid electrolytes (see Fig. S2).

Fig. 2 compares the formation rates of CO and H_2 of Ni-SAC-CNTs/GDE and Ag NPs/GDE as a function of the applied potential in electrolytes with various pHs from 0.5 to 14.0. Unless otherwise stated, all potentials are expressed on a pH-independent normal hydrogen electrode (NHE) scale. As clearly shown in Fig. 2a-b, the CO formation rates for both catalysts increase with the applied potential in the electrolyte with pH ≥ 2.0. This pH-independent CO formation rate originates from the fact that the rate-determining step (RDS) for the CO_2RR to CO is the first electron transfer process that does not involve H^+ [31,32].

While CO production is invariant with pH, HER shows a complicated pH- and material-dependence. In strong acids (pH 0.5 and 1.0), the H_2 formation rate increased with the applied potential and shifted to more negative potentials with increasing pH for both Ni-SAC-CNTs/GDE (Fig. 2d) and Ag NPs/GDE (Fig. 2c). This pH-dependent behavior is attributed to the direct reduction of H^+ to H_2 via the proton-coupled

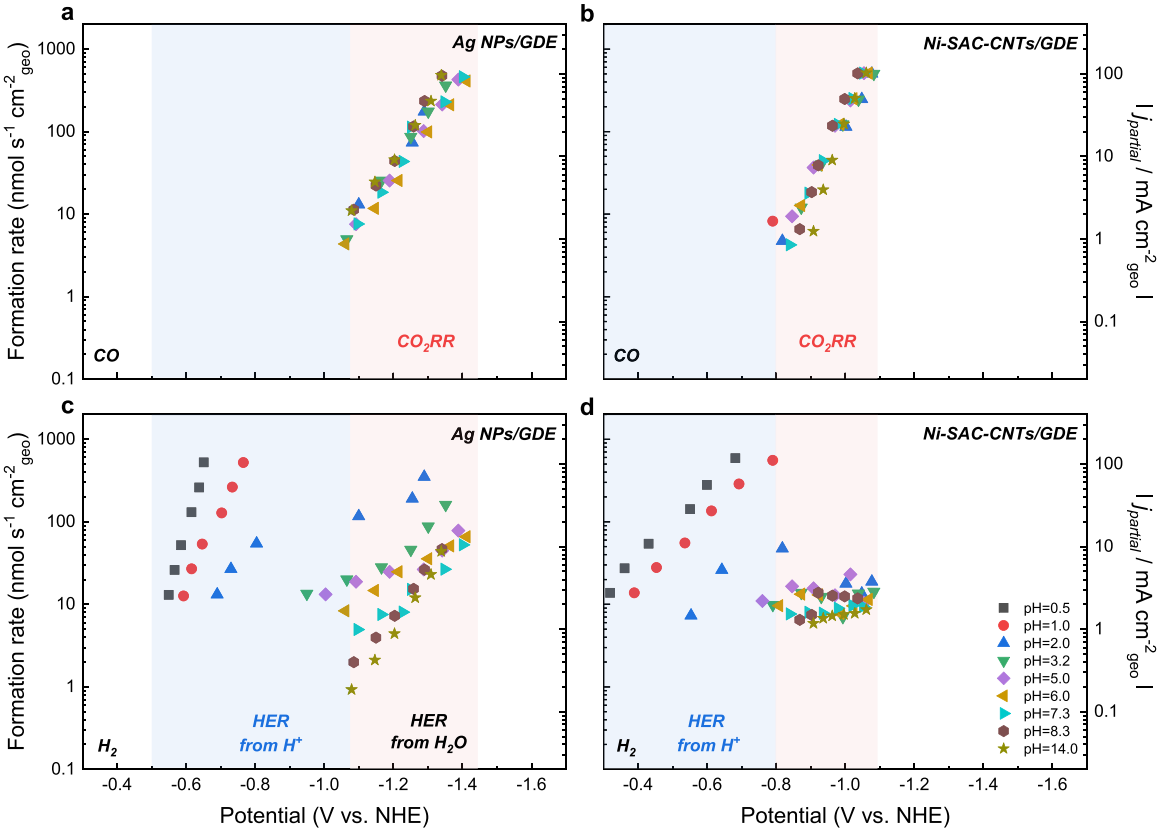

Fig. 2. Effect of pH on electrochemical CO_2RR and HER using Ag NPs and Ni-SAC-CNTs. (a and b) Formation rate (left y-axis) and corresponding partial current density (right y-axis) of CO product as a function of applied potential in various pH electrolyte for (a) Ag NPs/GDE and (b) Ni-SAC-CNTs/GDE. (c and d) Formation rate and corresponding partial current density of H_2 product as a function of applied potential in various pH electrolytes for (c) Ag NPs/GDE and (d) Ni-SAC-CNTs/GDE. In (a–d), each point was obtained by performing chronopotentiometry for 20 min under a nominal CO_2 flow rate of 20 sccm. Phosphate buffer electrolytes were used to set pH from 0.5 to 7.3, while pH 8.3 and 14.0 electrolytes were prepared by using $KHCO_3$ and KOH, respectively. Color codes indicate the potential windows for H^+ reduction reaction (light blue) and CO_2RR (light red).

electron transfer process:

$$2H^+ + 2e^- \rightarrow H_2 \quad (5)$$

At pH 2.0, Ni-SAC-CNTs/GDE continues to exhibit the anodic shift of HER at low potential; however, the HER rate quickly saturates as the overpotential increases from approximately −0.6 V to −0.8 V. This plateau region forms because [H^+] becomes locally deficient near the electrode, owing to an increase in the reaction rates in weak acids. Linear sweep voltammetry (LSV) established a characteristic peak for mass transfer-limited H^+ reduction in the corresponding potential region (Fig. S3). As the applied potential was further increased from −0.8 V, the HER rate of Ni-SAC-CNTs/GDE decreased from the plateau associated with the mass transfer limitation of H^+ and became nearly independent of the potential. In this potential range, the HER rate did not change with the pH (>2) of electrolytes, either. It should be noted that the suppression of the HER begins at the potential where CO_2RR is initiated (Fig. S4). CO_2RR releases OH^- and builds high local pH near the electrode by

$$CO_2 + H_2O + 2e^- \rightarrow CO + 2OH^- \quad (6)$$

The released OH^- quickly removes H^+ near the electrode via the neutralization reaction and thus suppresses the H^+ reduction reaction rate (Eq. 5) [22,25]. For example, when the galvanostatic CO_2RR was performed in a mild acid (e.g., ~pH 3) at −25 mA cm^{-2}_{geo}, the formation rate of CO was ~100 nmol s^{-1} cm^{-2}_{geo} at −1.0 V from Ni-SAC-CNTs/GDE (see Fig. 2b). Subsequently, OH^- is generated with the production rate of ~200 nmol s^{-1} cm^{-2}_{geo} via Eq. 6 and increases with applied potential. On the other hand, the maximum mass transfer rate of H^+ from the bulk to the cathode can be derived from the limiting current density equation (see Eq. S6 in *Note S2*) and is about 18 nmol s^{-1} cm^{-2}_{geo} at pH 3.0, independent of applied potential. Since the flux of OH^- in the bulk direction is much larger than that of H^+ to the cathode, the rate of OH^- generation is sufficient to offset the mass transfer of H^+ from the bulk electrolyte.

However, in the case of Ag NPs/GDE, the hydrogen formation rate surges at the potential where CO starts to evolve (Fig. 2c). The potential-dependent HER behavior indicates that the charge transfer (not the mass transfer) governs the overall HER kinetics. Besides, CO_2RR induces local alkalinity near the electrode, and H^+ is depleted near the Ag NPs/GDE. Therefore, the HER occurs through the H_2O reduction reaction:

$$2H_2O + 2e^- \rightarrow H_2 + 2OH^- \quad (7)$$

In addition to the much slower kinetics of H_2O reduction compared to H^+ reduction [33–35], the high free energies required to adsorb H of H_2O on the catalytic active sites lead to the harder activation of the H_2O reduction reaction [36–38]. In particular, for the catalyst with isolated active site (e.g., Ni-SAC-CNTs), it is important that the RDS (i.e., the initial adsorption) should be energetically favorable because H of H_2O and CO_2 would compete for occupying the single active site. Recently reported studies based on theoretical simulation exhibited that upon Ni single atom coordinated with nitrogens, the adsorption of CO_2 rather than that of H in H_2O is energetically preferable under a moderate negative potential applied [36,38]. The smaller free energy for CO_2

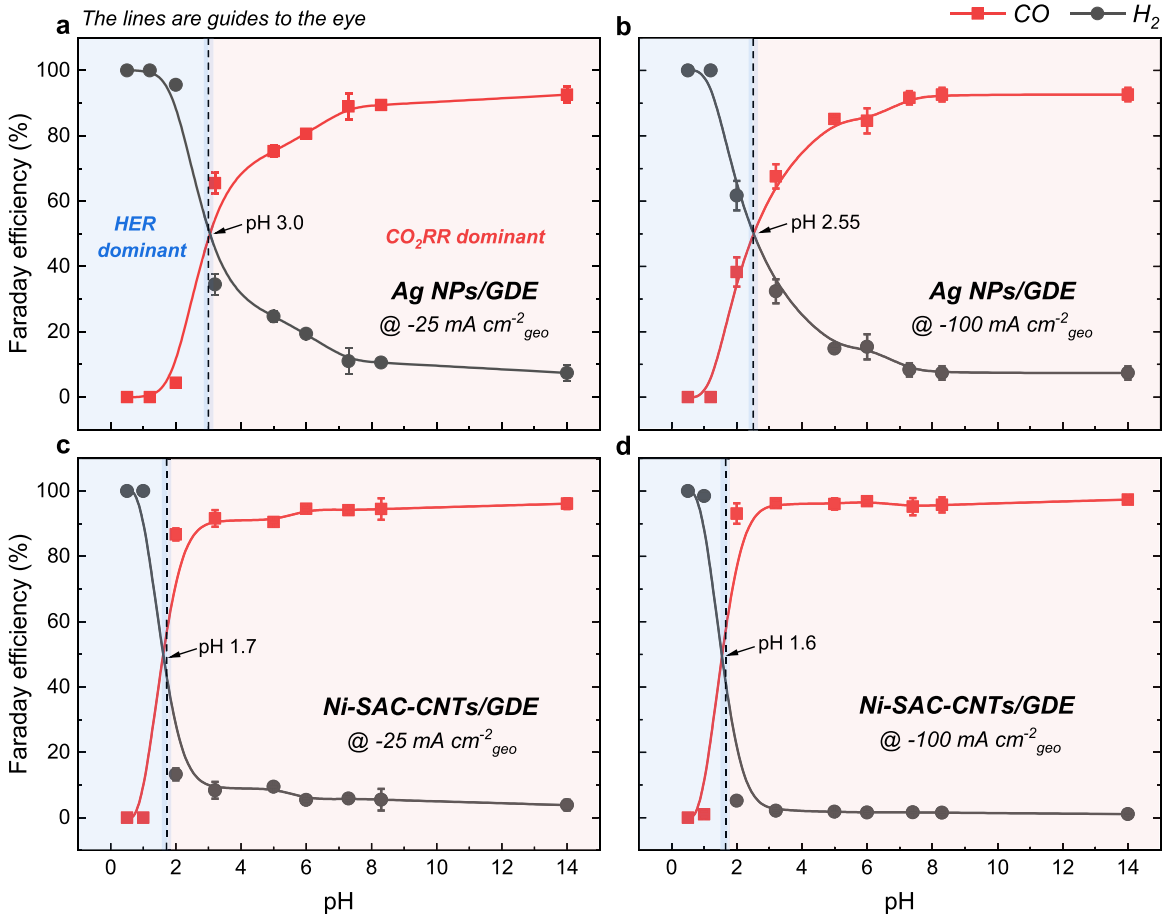

Fig. 3. Necessity of the high-performing catalyst for selective CO_2RR in an acid electrolyte. (a and b) Faraday efficiency (FE) of H_2 and CO as a function of electrolyte pH on Ag NPs/GDE under galvanostatic CO_2 electrolysis at (a) −25 mA cm^{-2}_{geo} and (b) −100 mA cm^{-2}_{geo}. (c and d) FE of H_2 and CO as a function of electrolyte pH on Ni-SAC-CNTs/GDE under galvanostatic CO_2 electrolysis at (c) −25 mA cm^{-2}_{geo} and (d) −100 mA cm^{-2}_{geo}. In (a–d), nominal CO_2 flow rate was 20 sccm and color codes indicate two pH regions where HER (light blue) or CO_2RR (light red) predominates. Data are represented as mean ± standard deviations from at least three independent tests if the error bars are presented.

adsorption indicates that CO_2RR (Eq. 6) becomes more dominant than the H_2O reduction reaction (Eq. 7). On the other hand, since Ag NPs require approximately 0.3–0.4 V more overpotential to drive CO_2RR, the H_2O reduction reaction can be sufficiently activated, indicating that the H_2O reduction reaction can partially or fully compete with CO_2RR (Fig. 2c-d).

The pH-dependent CO selectivity of Ag NPs/GDE and Ni-SAC-CNTs/GDE was obtained by comparing the CO and H_2 formation rates under the given electrolysis conditions. Fig. 3 shows the FEs for CO and H_2 in the two electrocatalysts as a function of the bulk pH at –25 and -100 mA cm^{-2}_{geo}. Because only CO and H_2 are produced during CO_2RR, CO FE represents the CO selectivity. Although Ag NPs/GDE selectivity produces CO with FE > 90% in neutral and alkaline solutions, H_2 evolution becomes dominant in solutions with pH < 3.0 at both current densities (Fig. 3a-b). For example, in the pH 2.0 electrolyte, the CO FE was only 5% at -25 mA cm^{-2}_{geo} and slightly increased to approximately 38% even at -100 mA cm^{-2}_{geo}. This poor CO selectivity of Ag NPs/GDE in mild acid results from the competition of CO_2RR with either H^+ reduction reaction at moderate potentials or the H_2O reduction reaction at large overpotentials (Fig. S5). In contrast, Ni-SAC-CNTs/GDE exhibited excellent CO FEs under acidic conditions (Fig. 3c-d). We achieved CO FEs over 80% and 90% at –25 and -100 mA cm^{-2}_{geo}, respectively, in the pH 2.0 electrolyte. The slight improvement in CO FE at pH 2.0 with increasing current density is consistent with our theoretical calculation and occurs due to the different electrochemical kinetics of CO_2RR and HER of Ni-SAC-CNTs in a gas-fed flow cell.

3.3. Effect of buffer capacity and alkali cations on electrochemical CO_2RR and HER in acids

Anions in electrolytes with different buffer capacity can influence CO_2RR and HER behaviors by changing local pH near an electrode [39, 40]. In order to explore the effect of buffering capacity of anions on CO_2RR and HER in acids, an 130 nm-thick Ag thin film formed by e-beam evaporator on a carbon paper-based GDE (Ag/GDE) was used as a model cathode. Fig. 4a-c show the electrochemical CO_2RR and HER characteristics of Ag/GDE in pH 2 electrolyte with sulfate and phosphate anions. As shown in Fig. 4a, the limiting current density for H^+ reduction is low in the presence of sulfate (non-buffer) unlike case of phosphate-based electrolyte (buffer solution). This low H^+ reduction limiting current from the sulfate-based electrolyte is attributed, in part, to elevated local pH by slow proton replenishment and endows selective CO production with ~93% FE even at low current density of -10 mA cm^{-2}_{geo} (Fig. 4b). In contrast, HER from H^+ reduction is dominant in a phosphate-based electrolyte at –10 and -25 mA cm^{-2}_{geo} due to its strong buffer capacity (Fig. 4c). At high current density where CO_2RR competes with H_2O reduction reaction, however, CO is produced selectively over H_2 in both electrolytes (Fig. 4b-c). Note that since both electrolytes have similar concentration of alkali cation, this difference is ascribed to the buffering effect of the anions.

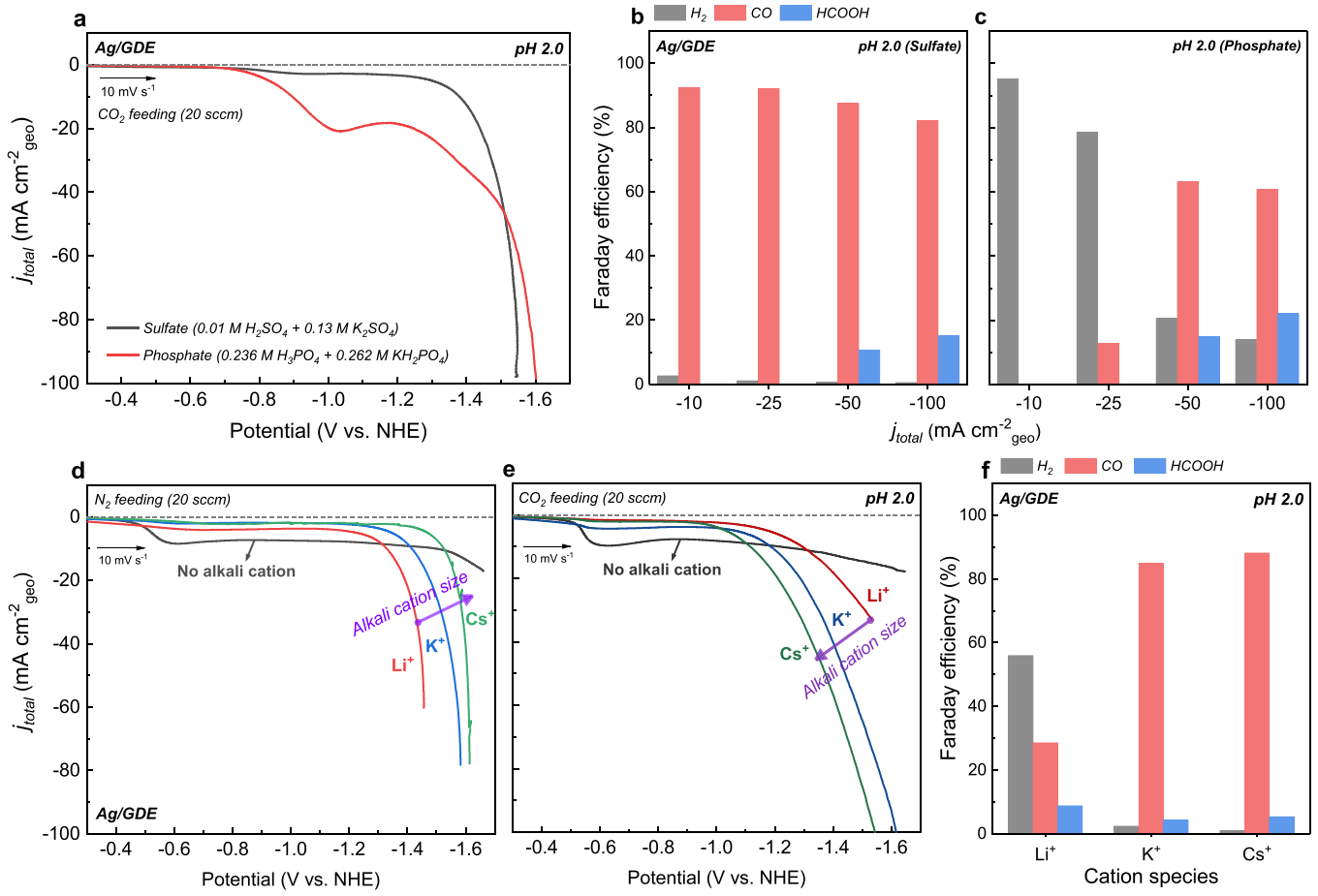

Fig. 4. Effect of buffer capacity and alkali cations on electrochemical CO_2RR and HER in acids. (a) *j-V* curves of Ag/GDE for electrochemical CO_2RR and HER in sulfate- and phosphate-based pH 2.0 electrolyte, respectively. The potential was scanned from − 0.3 V at a rate of 10 mV s^{-1} under a nominal CO_2 flow rate of 20 sccm and 95% iR-compensation was applied. (b and c) FE of H_2, CO, and HCOOH over Ag/GDE as a function of applied *j* in (b) sulfate- and (c) phosphate-based electrolyte. (d and e) *j-V* curves of Ag/GDE for electrochemical CO_2RR and HER in sulfate-based pH 2.0 electrolyte with (or without) various alkali metal cations under (d) N_2 and (e) CO_2 feeding conditions. Note that each nominal gas flow rate was 20 sccm and the potential was 95% iR-corrected. (f) FE of H_2, CO, and HCOOH over Ag/GDE depending on alkali metal cation species in sulfate-based pH 2.0 electrolyte at a constant current density of -100 mA cm^{-2}_{geo}.

Recently, it is reported that the alkali cations in electrolytes influence the interfacial charge transfer kinetics for HER [41–43] and CO_2RR [44, 45]. Fig. 4d shows the LSV curves in pH 2 electrolyte with various cations under the N_2 feeding condition. As discussed earlier, H^+ reduction occurs at low overpotential but its current is quickly limited by mass transfer in pH 2 electrolyte. At higher overpotential, H_2O is reduced to H_2 with its rate growing exponentially to the applied potential. As the larger cations are used, (1) the limiting current densities associated with H^+ reduction reaction are decreased and (2) the onset potentials for H_2O reduction in the higher cathodic potential shift to more negative direction. The presence of large alkali metal cations such as Cs^+ at the electrified interface in acids is suggested to expel interfacial H_2O molecules and render larger entropic barrier for the dissociation of H^+ from H_2O, leading to slow kinetics of H_2O reduction reaction [43]. In contrast, the *j-V* curves show dramatically different cation-dependent behavior in the CO_2 feeding environment. While the trend in limiting current for H^+ reduction is similar, the exponentially growing current densities at the higher overpotential shift to more anodic direction as the alkali cation sizes are increased (Fig. 4e). Since the current at high overpotential is associated with CO_2RR, the *j-V* curves indicate the promotion of CO_2RR by large cations. The recent theoretical study suggested that the weakly hydrated cation such as Cs^+ adsorbed on a catalyst induces the surface charges that promote CO_2RR [45].

Fig. 4f shows the product distribution of CO_2RR in pH 2 electrolytes with 0.26 M Li^+, K^+, and Cs^+ at -100 mA cm^{-2}_{geo}. When Li^+ is used, electrochemical HER is more favorable over CO_2RR, whereas CO production is dominant when a larger cation such as K^+ and Cs^+ is present in the solution (Fig. 4f). This is consistent with the LSV curves in Fig. 4d-e. These results indicate that the presence of alkali cation enables selective CO_2RR in an acidic environment by changing the interfacial electro-kinetics of competitive CO_2 and H_2O reduction reactions.

Fig. 5 summarizes three design principles for selective electrochemical CO_2-to-CO conversion under acidic conditions. In a gas-fed flow cell, CO_2RR competes with H_2O reduction at an industry-relevant current density. H_2 formation by H^+ reduction deteriorates CO_2RR selectivity only at low current density due to the mass transfer limit of H^+ in a mild acid. Hence, a catalyst with excellent intrinsic CO selectivity is effective because it shifts the j_{CO}–*V* curve to the anodic direction and j_{CO} prevails over j_{H2O} at high overpotential. Alkali metal cations such as K^+ and Cs^+ have the similar effects for a given catalyst as they promote CO_2RR at lower potential in addition to suppression of H_2O reduction reaction. However, the buffer capacity of electrolytes does not make CO_2 reduction selective over H_2 production at high current density. Instead, electrolyte with weak buffering capacity supports high CO selectivity at low current densities where CO_2RR competes with H^+ reduction reaction.

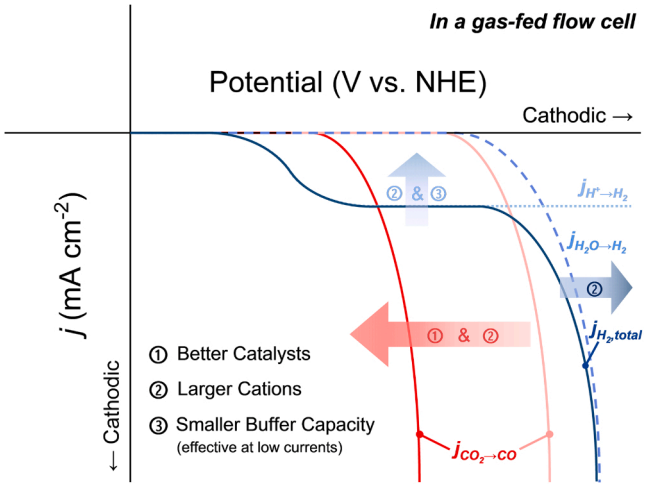

Fig. 5. Summary plot of design principles for selective CO_2RR in acids. Schematic *j-V* curves for electrochemical CO_2RR and HER under various reaction conditions, showing three design principles to achieve selective CO_2-to-CO reaction in an acid electrolyte using a CO_2-fed flow cell.

3.4. *High CO_2-to-CO single-pass conversion from acidic CO_2RR in a flow cell*

We systematically investigated the influence of various CO_2RR electrolysis operation parameters on CO_2-to-CO SPC by using Ni-SAC-CNTs/GDE at industry-relevant current densities in acid electrolytes. Fig. 6a shows a schematic of the gas balance in the cathode compartment of a gas-fed flow cell (see Fig. S6 for the gas balance and relevant (electro-)chemical reactions). Part of the CO_2 supplied to the cathode compartment ($CO_{2,inlet}$) passes through the gas diffusion layer (GDL) and is consumed by two reactions within the catalyst layer (CL): (1) electrochemical CO_2-to-CO reaction and (2) non-electrochemical (non-EC) reactions to form CO_2(aq), HCO_3^-, and CO_3^{2-}. The produced CO flowed downstream into the gas chamber. The outlet gases include H_2 and unreacted CO_2. CO_2 for non-EC reactions is dissolved in the catholyte and thus vanishes from the gas flow.

Fig. 6b shows the CO_2 loss associated with non-EC reactions as a function of the CO_2RR current density in electrolytes with different pH values. It is evident that large amounts of CO_2 are lost by the chemical reaction with OH^- in electrolytes of high pH. The slight decrease in the outlet gas flow at pH 2.0 in the open-circuit condition corresponds to the dissolution of CO_2 in the form of CO_2(aq), which is independent of the pH of the electrolyte. As CO_2RR is driven at a higher current density, the non-EC loss becomes greater in all electrolytes. This is because of the accelerated formation of HCO_3^- and CO_3^{2-} that occurs due to the high local alkalinity near the electrode (Eq. S13a-b in *Note S3*) during CO_2RR. However, the degree of non-EC loss in the acid electrolyte is less than that in neutral and alkaline electrolytes: H^+ migrated from the bulk solution compensates/neutralizes the OH^- by-products and limits the local pH to rise at/near the electrode (see Fig. S7 for the schematics). The pH of the flooded catholyte through the GDE was approximately 8, whereas the pH of the bulk catholyte remained at approximately 2 after prolonged CO_2RR (Fig. S8). This local pH of approximately 8 suppressed the formation of CO_3^{2-} and minimized the non-EC loss, even at a high CO_2RR current density (Fig. 1a). It should be noted that the limited local alkalinity prohibits carbonate salt precipitation on the cathode surface after CO_2RR in acidic conditions (Fig. S9). The absence of carbonate salt precipitation on the electrode would allow stable electrolysis using Ni-SAC-CNTs/GDE for at least 10 h in the pH 2.0 electrolyte (Fig. S10). Note that changes in the morphology and elemental distribution of Ni-SAC-CNTs were negligible after prolonged CO_2RR (Fig. S11). Since an industrial electrolysis system often requires stable operation for more than 1000 h, however, further evaluations are needed to investigate whether the performance of our catalysts is degraded through the morphology change and/or Ni leaching out after industry-relevant stability testing.

Fig. 6c shows the distribution of the consumed $CO_{2,inlet}$ as a function of the CO_2 flow rate in electrolytes with different pH values at -100 mA cm^{-2}_{geo} (see *Note S3* for the detailed balance equation). As clearly seen in Fig. 6c, decreasing the CO_2 flow rate dramatically enhanced the consumption rate of the fed CO_2 into the EC and non-EC reactions. CO_2 to non-EC reactions can be minimized in acids, and the fraction of the EC reaction (i.e., CO_2-to-CO SPC) increases as the pH decreases. As CO selectivity is maintained $>$ 90% even at a low CO_2 flow rate of 2.1 standard cubic centimeters per minute (sccm) in all pH electrolytes (Fig. S12), the CO_2-to-CO SPC at pH 2.0 reaches about 60% under a CO_2 flow rate of 2.1 sccm. This is about 10% higher SPC than that achieved at pH 8.3. The CO_2-to-CO SPC could not be measured at pH 14.0, owing to the unavoidable flooding.

To further increase the CO_2-to-CO SPC, a higher current density was applied to the Ni-SAC-CNTs/GDE in the electrolyte (pH 2.0) (Fig. 6d). A CO selectivity of higher than 93% was maintained even at -200 mA cm^{-}

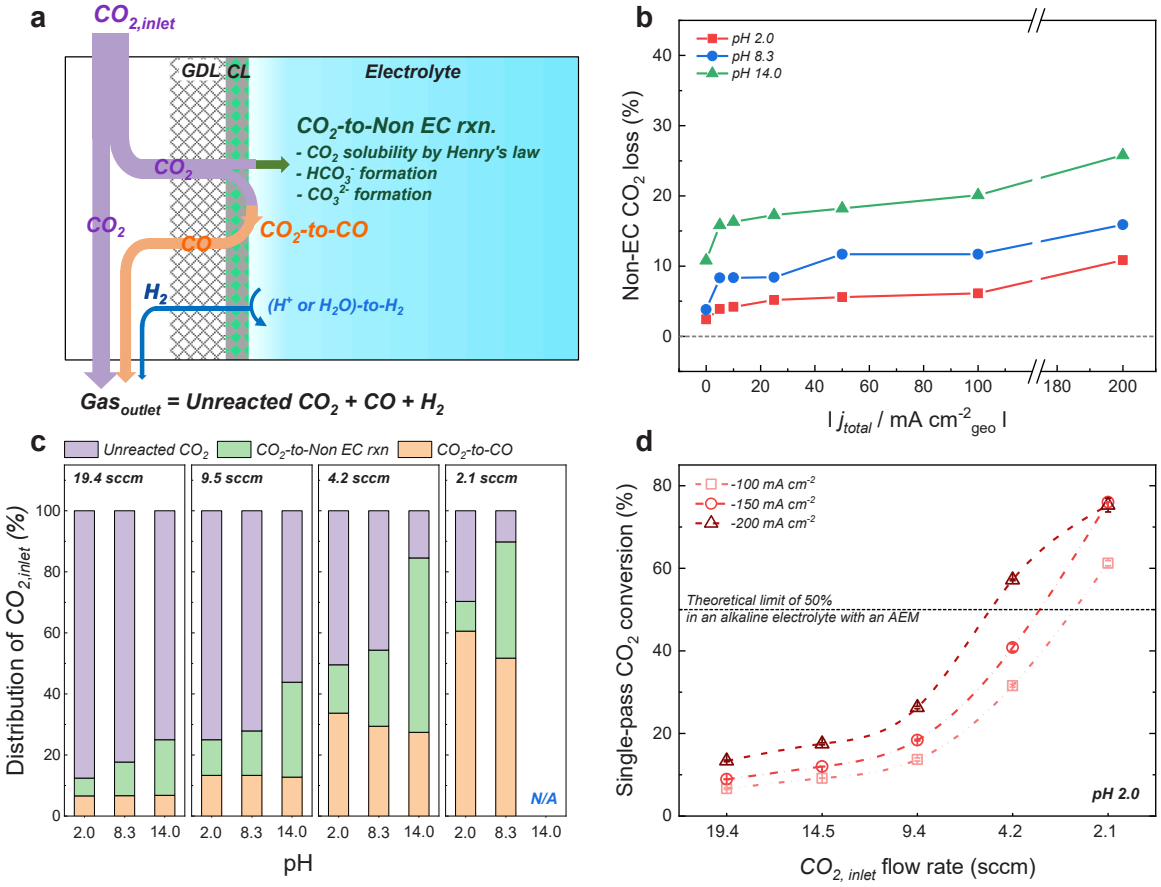

Fig. 6. Advantages of using acid electrolytes for CO_2 electrolysis in a gas-fed flow cell. (a) Schematic illustration of gas flow rate-based mass balance in a cathode compartment of gas-fed flow cell. GDL and CL indicated in (a) are abbreviations for gas diffusion layer and catalyst layer, respectively; (b) Fraction of CO_2 loss through non-electrochemical (non-EC) reactions as a function of CO_2RR current density in various pH electrolytes; (c) Carbon balance for the inlet CO_2 flow during CO_2 electrolysis at a constant current density of −100 mA cm^{-2}_{geo} in various pH electrolytes at various CO_2 flow rates. (d) CO_2-to-CO single-pass conversion at various CO_2 flow rates at different current densities in pH 2.0 electrolyte. For all experiments, Ni-SAC-CNTs/GDEs were used. Data are represented as mean ± standard deviations from at least three independent tests if the error bars are presented.

$^{2}_{geo}$ under various CO_2 flow rates (except 2.1 sccm) (Fig. S13). As shown in Fig. 6d, we achieved approximately 77% of the CO_2-to-CO SPC when the applied current density was above −150 mA cm^{-2}_{geo} at a pH 2.0 and CO_2 flow rate of 2.1 sccm. To the best of our knowledge, this SPC value is the highest for the CO_2-to-CO conversion without additional engineering for controlling local reaction environments (Table S1). It should be noted that the SPC was limited to about 77% even when the current density was increased to −200 mA cm^{-2}_{geo}. This was mainly due to the degraded CO selectivity at −200 mA cm^{-2}_{geo} under a CO_2 flow rate of 2.1 sccm, and partly due to the depleted [CO_2] at/near the electrode (Fig. S13). Several bubbles are released from the cathode, with periodic potential fluctuations being observed during chronopotentiometry in the pH 2.0 electrolyte (see Fig. S14 and S15). The bubbles are CO_2 regenerated from HCO_3^- and/or CO_3^{2-} in the bulk pH 2.0 electrolyte [22,46,47]. If the regenerated CO_2 can be recycled for CO_2RR at the cathode, we believe that the SPC can be further enhanced [48].

3.5. Techno-economic and life cycle assessments of CO_2RR processes

Although Ni-SAC-CNTs show high SPC in acid, pH-independent CO formation degrades the cathodic energy efficiency (Fig. S16) and can limit the environmental and economic impact of the Ni-SAC-CNTs-catalyzed acidic CO_2RR. Thus, we conducted and compared the techno-economic assessment (TEA) and life cycle assessment (LCA) of the acid and alkaline electrolytes based on the electrolyzer performance and carbon balance (see *Note S4,* Table S2-S6 and *Note for* Table S2). The cost of goods manufactured (COGM), i.e., CO in our case, and the (partial) carbon footprint of the designed processes were analyzed based on the CO_2RR system, which includes an electrolyzer, unreacted CO_2 recovery process, and electrolyte regeneration (Fig. S17).

As shown in Fig. 7, acidic and alkaline CO_2 electrolysis systems have similar economics in our baseline scenario (i.e., the South Korea case); however, the carbon footprint of the alkaline CO_2 electrolysis is unexpectedly lower than that of the acidic CO_2RR at the baseline electricity price (100.3 USD MWh^{-1}) and GWI (Table S7). Despite the high SPC and minimal carbonate crossover, the fundamental 59 mV pH^{-1} energy penalty of the acidic CO_2RR requires the use of a larger amount of electricity, which nullifies the economic and environmental advantages of minimizing the CO_2 recovery and electrolyte regeneration processes (Table S8 and S10). Conversely, Norway primarily utilizes renewable energy for power generation; thus, electricity prices (68.1 USD MWh^{-1}) and GWI are significantly lower than those of South Korea. Although the techno-economics for the acidic/alkaline CO_2 electrolysis is similar in both countries (Fig. 7a), indirect greenhouse gas (GHG) emissions from the electricity used are dramatically lower in Norway, leading to significantly lower carbon footprint compared to those for the alkaline CO_2 electrolysis (Fig. 7b, Table S9 and S11). Therefore, utilizing less carbon-intensive electricity can change the environmental superiority of the electrolyte, as observed in Norway scenario.

Fig. 8 shows the local sensitivity analysis results with respect to electrolyzer performance parameters, e.g., the cell voltage and SPC, and non-technical parameters, e.g., prices and GWI of electricity, to examine

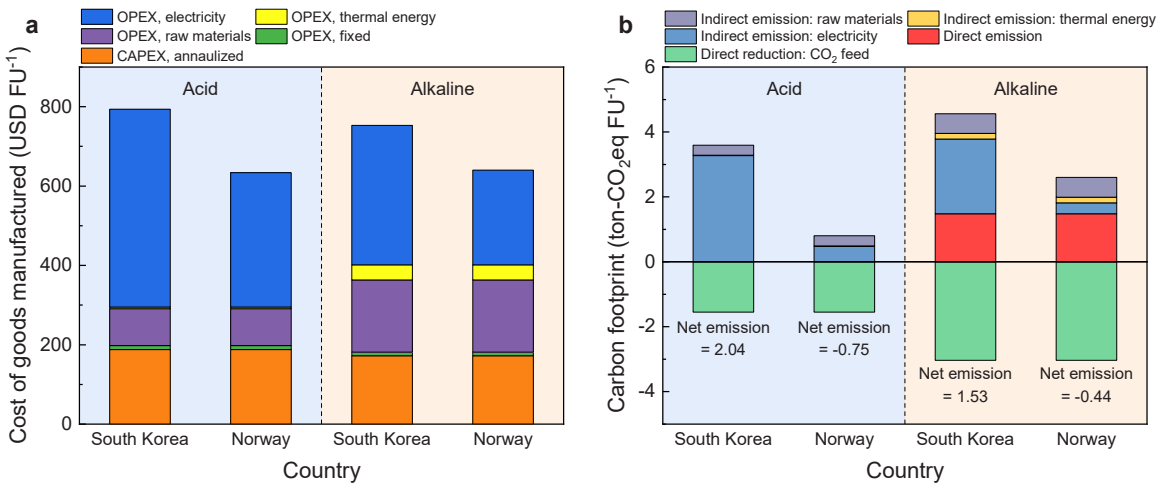

Fig. 7. TEA/LCA results in the South Korea/Norway scenarios. (a) TEA results in South Korea and Norway scenarios. The functional unit (FU) is one ton of 97 wt% CO product and the COGM is composed of capital expenditure (CAPEX) and operating expenditures (OPEX). CAPEX is an annualized total capital investment considering the project year and discount factor. OPEX are categorized into three components such as 'utilities', 'raw materials', and 'fixed'. In our TEA, the electricity and steam (i.e., thermal energy) are considered as the two major components of utilities, and CO_2 and an amine solvent (for CO_2 recovery) as important raw materials. Fixed OPEX are costs that must be spent regardless of process operation: labor, maintenance, administration, overhead costs, etc. Note that the price of electricity for South Korea scenario is based on 100.3 USD MWh^{-1}, and that for Norway scenario is 68.1 USD MWh^{-1} [49]. (b) The LCA results in South Korea and Norway scenarios, respectively. Indirect GHG emissions from raw materials and energy acquisition as well as direct emission highly depend on the pH of electrolyte of CO_2RR. Direct emission is discharge of the CO_2 at the anode outlet stream during CO_2RR in the alkaline case. Using less carbon-intensive electricity can take advantage of acid electrolytes.

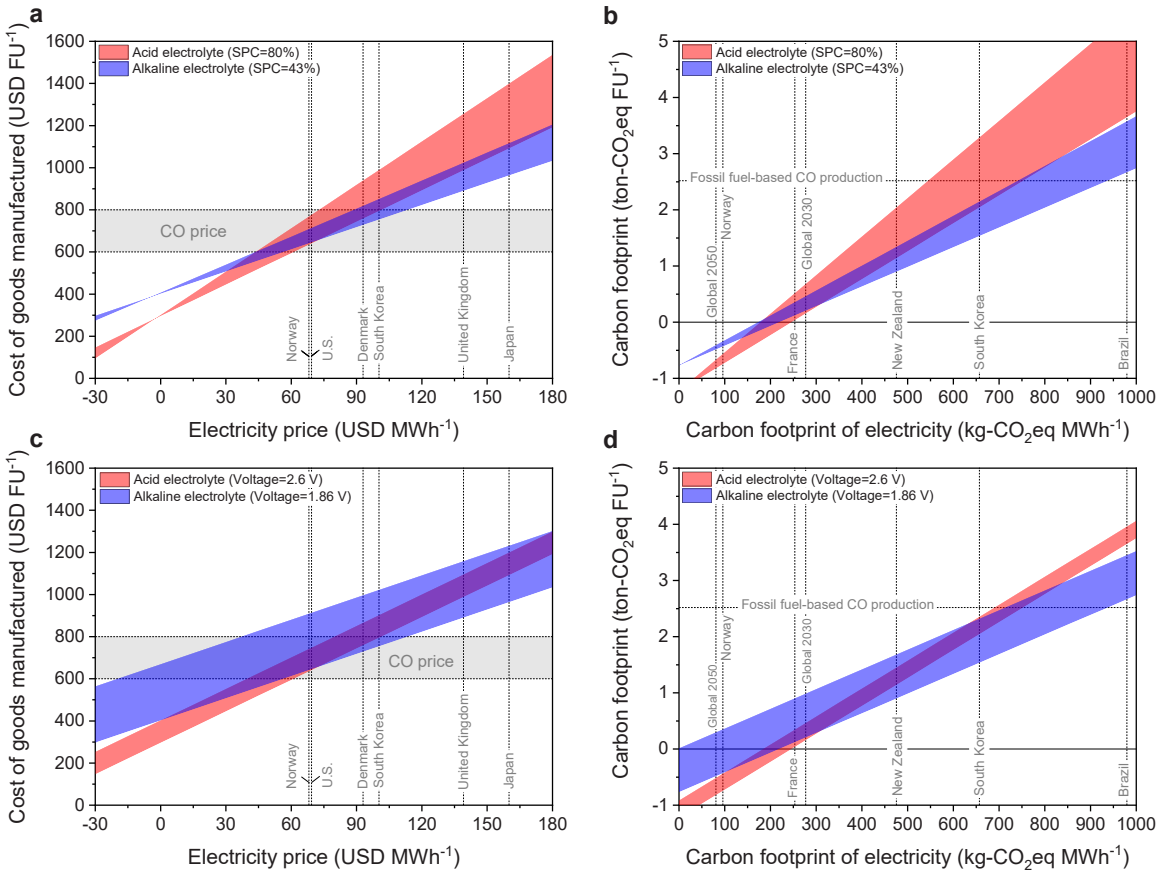

Fig. 8. Sensitivity analysis of COGM and carbon footprint with respect to the key electrolyzer performances, and the price and GWI of electricity. Sensitivity analysis of COGM and carbon footprint with respect to cell voltage (a and b) and SPC (c and d). The upper and lower bounds of the color-coded regime in the plot correspond to the lowest and highest SPC and cell voltages, respectively. The price of CO is given as an interval [7,50]: Fossil fuel-based CO production is based on steam methane reforming technology. A negative price of electricity indicates financial compensation when offering ancillary services on demand to balance the power grid.

their influences on the COGM and carbon footprint under each electrolyte condition. The economic and environmental performances under the acidic conditions are more influenced by the price and GWI of electricity than those under the alkaline conditions. Conversely, low SPC under the alkaline conditions demands a large amount of steam consumption for CO_2 recovery. Thus, the performance indicators of the alkaline case are more influenced by the price and GWI of steam than by the acidic condition (see Fig. S18). Hence, as shown in Figs. 8a and 8c, the acidic CO_2RR would be more favorable than the alkaline one if surplus or cheap renewable electricity is available. From the perspective of GHG reduction, acid electrolytes would be appropriate for regions with abundant renewable energy resources (e.g., Iceland and Norway) or in the future scenario when more renewable energy penetrates the power grid (Fig. 8b and d, and Table S12).

4. Conclusions

We provided design principles for highly selective and economical electrochemical conversion of CO_2-to-CO in an acid electrolyte (pH 2.0) in a gas-fed flow cell. While a gas-fed flow cell warrants inherent CO production over the H^+ reduction reaction in an acid, a catalyst is required to have high intrinsic CO selectivity to avoid competition with the H_2O reduction reaction. Consequently, the high-performance Ni-SAC-CNTs/GDE exhibited a CO FE of approximately 93% at -100 mA cm^{-2}_{geo}, whereas commercial Ag NPs/GDE predominantly produced H_2 via the H_2O reduction reaction at an electrolyte of pH 2.0. We also identify the role of cation and anions specie in electrolyte on selective CO_2RR over HER: large alkali metal cations can modulate the interfacial kinetics of CO_2 and H_2O reduction reactions for selective CO production at high current density while anions are only effective for H^+ reduction reaction at low current density. Finally, the selective CO production from Ni-SAC-CNTs/GDE in acid enables the highest CO_2-to-CO SPC of up to 77% by minimizing non-EC CO_2 loss from the suppression of HCO_3^- and/or CO_3^{2-} formation. As a result of TEA and LCA, we identified the conditions under which the acid electrolyte may be advantageous over the alkaline electrolyte. As more renewable energy resources penetrate the power grid over time, acid electrolytes are expected to become more suitable for GHG reduction through CO_2RR than alkaline electrolytes. Although further efforts are still needed for designing and optimizing large-scale CO_2 electrolyzers, such as a membrane electrode assembly with a cation exchange membrane, our work will provide new insights to future studies on efficient and economical electrochemical CO_2RR.

CRediT authorship contribution statement

Jaehoon Kim, **Tae Hyeon Ha**, and **Jihun Oh** conceived the project, contributed to the analysis and discussion of the data, and wrote the manuscript. **Jaehoon Kim** designed the experiments and performed theoretical calculations. **Tae Hyeon Ha** and **Gyoung Hwa Jeong** synthesized and characterized the materials. **Jaehoon Kim** and **Tae Hyeon Ha** performed the electrochemical tests and analysis. **Junehyeok Kim** and **Kosan Roh** contributed to the process design based on MATLAB environment and techno-economic/life-cycle assessments, and wrote the manuscript. **Wonsuk Chung** designed the amine scrubbing process. **Sang Ouk Kim** and **Jihun Oh** provided expertise and feedback. **Jay H. Lee** and **Jihun Oh** secured funding and supervised the project. All authors have reviewed the manuscript.

Declaration of Competing Interest

The authors declare the following financial interests/personal relationships which may be considered as potential competing interests: Jihun Oh reports financial support was provided by Korea Ministry of Science and ICT. Jay H. Lee reports financial support was provided by Korea Ministry of Science and ICT. Sang Ouk Kim reports financial support was provided by Korea Ministry of Science and ICT. Kosan Roh reports financial support was provided by Korea Ministry of Science and ICT.

Data availability

All the data presented in this study are available from the corresponding authors upon request.

Acknowledgments

This work was supported by the “Carbon to X Project” (NRF-2020M3H7A1096388 and NRF-2020M3H7A1096361) and the National Creative Research Initiative (CRI) Center for Multi-Dimensional Directed Nanoscale Assembly (2015R1A3A2033061) and Education Center for Energy, Environment, and Climate Technologies (ECEECT, grant No. 2022M3J7A1066428) through the National Research Foundation (NRF) funded by the Ministry of Science and ICT (MSIT), Republic of Korea. This work was also supported by the National Research Council of Science & Technology (NST) grant by the MSIT (No. CRC22042–400).

Appendix A. Supporting information

Supplementary data associated with this article can be found in the online version at doi:10.1016/j.apcatb.2023.123160.

References

[1] P. De Luna, C. Hahn, D. Higgins, S.A. Jaffer, T.F. Jaramillo, E.H. Sargent, What would it take for renewably powered electrosynthesis to displace petrochemical processes? Science 364 (2019) eaav3506, https://doi.org/10.1126/science.aav3506.
[2] S. Nitopi, E. Bertheussen, S.B. Scott, X. Liu, A.K. Engstfeld, S. Horch, B. Seger, I. E. Stephens, K. Chan, C. Hahn, Progress and perspectives of electrochemical CO_2 reduction on copper in aqueous electrolyte, Chem. Rev. 119 (2019) 7610–7672, https://doi.org/10.1021/acs.chemrev.8b00705.
[3] Y. Zhang, G. Jacobs, D.E. Sparks, M.E. Dry, B.H. Davis, CO and CO_2 hydrogenation study on supported cobalt Fischer–Tropsch synthesis catalysts, Catal. Today 71 (2002) 411–418, https://doi.org/10.1016/S0920-5861(01)00468-0.
[4] M. Cho, J.-W. Seo, J.T. Song, J.-Y. Lee, J. Oh, Silver nanowire/carbon sheet composites for electrochemical syngas generation with tunable H_2/CO ratios, ACS Omega 2 (2017) 3441–3446, https://doi.org/10.1021/acsomega.7b00846.
[5] M. Jouny, G.S. Hutchings, F. Jiao, Carbon monoxide electroreduction as an emerging platform for carbon utilization, Nat. Catal. 2 (2019) 1062–1070, https://doi.org/10.1038/s41929-019-0388-2.
[6] Y. Han, Z. Wang, X. Han, W. Fang, Y. Zhou, K. Lei, B. You, H.S. Park, B.Y. Xia, Selectively converting carbon dioxide to syngas over intermetallic AuCu catalysts, ACS Sustain. Chem. Eng. 9 (2021) 2609–2615, https://doi.org/10.1021/acssuschemeng.0c09146.
[7] M. Jouny, W. Luc, F. Jiao, General techno-economic analysis of CO_2 electrolysis systems, Ind. Eng. Chem. Res. 57 (2018) 2165–2177, https://doi.org/10.1021/acs.iecr.7b03514.
[8] C.-T. Dinh, Y.C. Li, E.H. Sargent, Boosting the single-pass conversion for renewable chemical electrosynthesis, Joule 3 (2019) 13–15, https://doi.org/10.1016/j.joule.2018.10.021.
[9] T. Burdyny, W.A. Smith, CO_2 reduction on gas-diffusion electrodes and why catalytic performance must be assessed at commercially-relevant conditions, Energy Environ. Sci. 12 (2019) 1442–1453, https://doi.org/10.1039/C8EE03134G.
[10] Y.C. Tan, K.B. Lee, H. Song, J. Oh, Modulating local CO_2 concentration as a general strategy for enhancing C−C coupling in CO_2 electroreduction, Joule 4 (2020) 1104–1120, https://doi.org/10.1016/j.joule.2020.03.013.
[11] S. Verma, X. Lu, S. Ma, R.I. Masel, P.J. Kenis, The effect of electrolyte composition on the electroreduction of CO_2 to CO on Ag based gas diffusion electrodes, Phys. Chem. Chem. Phys. 18 (2016) 7075–7084, https://doi.org/10.1039/C5CP05665A.
[12] S. Verma, Y. Hamasaki, C. Kim, W. Huang, S. Lu, H.-R.M. Jhong, A.A. Gewirth, T. Fujigaya, N. Nakashima, P.J. Kenis, Insights into the low overpotential electroreduction of CO_2 to CO on a supported gold catalyst in an alkaline flow electrolyzer, ACS Energy Lett. 3 (2017) 193–198, https://doi.org/10.1021/acsenergylett.7b01096.
[13] C.M. Gabardo, A. Seifitokaldani, J.P. Edwards, C.-T. Dinh, T. Burdyny, M.G. Kibria, C.P. O’Brien, E.H. Sargent, D. Sinton, Combined high alkalinity and pressurization enable efficient CO_2 electroreduction to CO, Energy Environ. Sci. 11 (2018) 2531–2539, https://doi.org/10.1039/C8EE01684D.
[14] G.H. Jeong, Y.C. Tan, J.T. Song, G.-Y. Lee, H.J. Lee, J. Lim, H.Y. Jeong, S. Won, J. Oh, S.O. Kim, Synthetic multiscale design of nanostructured Ni single atom

catalyst for superior CO_2 electroreduction, Chem. Eng. J. 426 (2021), 131063, https://doi.org/10.1016/j.cej.2021.131063.
[15] J.J. Lv, M. Jouny, W. Luc, W. Zhu, J.J. Zhu, F. Jiao, A highly porous copper electrocatalyst for carbon dioxide reduction, Adv. Mater. 30 (2018), 1803111, https://doi.org/10.1002/adma.201803111.
[16] E.R. Cofell, U.O. Nwabara, S.S. Bhargava, D.E. Henckel, P.J. Kenis, Investigation of electrolyte-dependent carbonate formation on gas diffusion electrodes for CO_2 electrolysis, ACS Appl. Mater. Interfaces 13 (2021) 15132–15142, https://doi.org/10.1021/acsami.0c21997.
[17] J.A. Rabinowitz, M.W. Kanan, The future of low-temperature carbon dioxide electrolysis depends on solving one basic problem, Nat. Commun. 11 (2020) 1–3, https://doi.org/10.1038/s41467-020-19135-8.
[18] J. Gu, S. Liu, W. Ni, W. Ren, S. Haussener, X. Hu, Modulating electric field distribution by alkali cations for CO_2 electroreduction in strongly acidic medium, Nat. Catal. 5 (2022) 1–9, https://doi.org/10.1038/s41929-022-00761-y.
[19] C. Chen, Y. Li, P. Yang, Address the "alkalinity problem" in CO_2 electrolysis with catalyst design and translation, Joule 5 (2021) 737–742, https://doi.org/10.1016/j.joule.2021.02.008.
[20] E. Jeng, F. Jiao, Investigation of CO_2 single-pass conversion in a flow electrolyzer, React. Chem. Eng. 5 (2020) 1768–1775, https://doi.org/10.1039/D0RE00261E.
[21] G.O. Larrazábal, M. Ma, B. Seger, A. Comprehensive, Approach to investigate CO_2 reduction electrocatalysts at high current densities, Acc. Mater. Res 2 (2021) 220–229, https://doi.org/10.1021/accountsmr.1c00004.
[22] J.E. Huang, F. Li, A. Ozden, A. Sedighian Rasouli, F.P. García de Arquer, S. Liu, S. Zhang, M. Luo, X. Wang, Y. Lum, CO_2 electrolysis to multicarbon products in strong acid, Science 372 (2021) 1074–1078, https://doi.org/10.1126/science.abg6582.
[23] J. Li, N. Kornienko, Electrocatalytic carbon dioxide reduction in acid, Chem. Catal. 2 (2021) 29–38, https://doi.org/10.1016/j.checat.2021.10.016.
[24] M.C. Monteiro, M.F. Philips, K.J.P. Schouten, M. Koper, Efficiency and selectivity of CO_2 reduction to CO on gold gas diffusion electrodes in acidic media, Nat. Commun. 12 (2021) 1–7, https://doi.org/10.1038/s41467-021-24936-6.
[25] C.J. Bondue, M. Graf, A. Goyal, M.T. Koper, Suppression of hydrogen evolution in acidic electrolytes by electrochemical CO_2 reduction, J. Am. Chem. Soc. 143 (2020) 279–285, https://doi.org/10.1021/jacs.0c10397.
[26] Z. Jiang, Z. Zhang, H. Li, Y. Tang, Y. Yuan, J. Zao, H. Zheng, Y. Liang, Molecular Catalyst with Near 100% Selectivity for CO_2 Reduction in Acidic Electrolytes, Adv. Energy Mater. (2022), 2203603, https://doi.org/10.1002/aenm.202203603.
[27] B. Pan, J. Fan, J. Zhang, Y. Luo, C. Shen, C. Wang, Y. Wang, Y. Li, Close to 90% Single-Pass Conversion Efficiency for CO_2 Electroreduction in an Acid-Fed Membrane Electrode Assembly, ACS Energy Lett. 7 (2022) 4224–4231, https://doi.org/10.1021/acsenergylett.2c02292.
[28] D.W. Keith, G. Holmes, D.S. Angelo, K. Heidel, A process for capturing CO_2 from the atmosphere, Joule 2 (2018) 1573–1594, https://doi.org/10.1016/j.joule.2018.05.006.
[29] R. Sinnott, G. Towler. Chemical engineering design, SI edition.,, Butterworth-Heinemann, 2019.
[30] F. Roughton, The kinetics and rapid thermochemistry of carbonic acid, J. Am. Chem. Soc. 63 (1941) 2930–2934, https://doi.org/10.1021/ja01856a018.
[31] A.S. Varela, M. Kroschel, N.D. Leonard, W. Ju, J. Steinberg, A. Bagger, J. Rossmeisl, P. Strasser, pH effects on the selectivity of the electrocatalytic CO_2 reduction on graphene-embedded Fe–N–C motifs: bridging concepts between molecular homogeneous and solid-state heterogeneous catalysis, ACS Energy Lett. 3 (2018) 812–817, https://doi.org/10.1021/acsenergylett.8b00273.
[32] S. Ringe, C.G. Morales-Guio, L.D. Chen, M. Fields, T.F. Jaramillo, C. Hahn, K. Chan, Double layer charging driven carbon dioxide adsorption limits the rate of electrochemical carbon dioxide reduction on Gold, Nat. Commun. 11 (2020) 1–11, https://doi.org/10.1038/s41467-019-13777-z.
[33] D. Strmcnik, M. Uchimura, C. Wang, R. Subbaraman, N. Danilovic, D. Van Der Vliet, A.P. Paulikas, V.R. Stamenkovic, N.M. Markovic, Improving the hydrogen oxidation reaction rate by promotion of hydroxyl adsorption, Nat. Chem. 5 (2013) 300–306, https://doi.org/10.1038/nchem.1574.
[34] J. Rossmeisl, K. Chan, E. Skulason, M.E. Björketun, V. Tripkovic, On the pH dependence of electrochemical proton transfer barriers, Catal. Today 262 (2016) 36–40, https://doi.org/10.1016/j.cattod.2015.08.016.
[35] I. Ledezma-Yanez, W.D.Z. Wallace, P. Sebastián-Pascual, V. Climent, J.M. Feliu, M. Koper, Interfacial water reorganization as a pH-dependent descriptor of the hydrogen evolution rate on platinum electrodes, Nat. Energy 2 (2017) 1–7, https://doi.org/10.1038/nenergy.2017.31.
[36] M.D. Hossain, Y. Huang, T.H. Yu, W.A. Goddard III, Z. Luo, Reaction mechanism and kinetics for CO_2 reduction on nickel single atom catalysts from quantum mechanics, Nat. Commun. 11 (2020) 2256.
[37] H. Cao, Z. Zhang, J.-W. Chen, Y.-G. Wang, Potential-dependent free energy relationship in interpreting the electrochemical performance of CO_2 reduction on single atom catalysts, ACS Catal. 12 (2022) 6606–6617.
[38] H. Li, H. Li, P. Wei, Y. Wang, Y. Zang, D. Gao, G. Wang, X. Bao, Tailoring acidic microenvironments for carbon-efficient CO_2 electrolysis over a Ni–N–C catalyst in a membrane electrode assembly electrolyzer, Energy Environ. Sci. 16 (2023) 1502–1510.
[39] J. Resasco, Y. Lum, E. Clark, J.Z. Zeledon, A.T. Bell, Effects of anion identity and concentration on electrochemical reduction of CO_2, ChemElectroChem 5 (2018) 1064–1072, https://doi.org/10.1002/celc.201701316.
[40] M.N. Jackson, O. Jung, H.C. Lamotte, Y. Surendranath, Donor-dependent promotion of interfacial proton-coupled electron transfer in aqueous electrocatalysis, ACS Catal. 9 (2019) 3737–3743, https://doi.org/10.1021/acscatal.9b00056.
[41] E. Liu, J. Li, L. Jiao, H.T.T. Doan, Z. Liu, Z. Zhao, Y. Huang, K. Abraham, S. Mukerjee, Q. Jia, Unifying the hydrogen evolution and oxidation reactions kinetics in base by identifying the catalytic roles of hydroxyl-water-cation adducts, J. Am. Chem. Soc. 141 (2019) 3232–3239, https://doi.org/10.1021/jacs.8b13228.
[42] S. Xue, B. Garlyyev, S. Watzele, Y. Liang, J. Fichtner, M.D. Pohl, A.S. Bandarenka, Influence of alkali metal cations on the hydrogen evolution reaction activity of Pt, Ir, Au, and Ag electrodes in alkaline electrolytes, ChemElectroChem 5 (2018) 2326–2329, https://doi.org/10.1002/celc.201800690.
[43] B. Huang, R.R. Rao, S. You, K. Hpone Myint, Y. Song, Y. Wang, W. Ding, L. Giordano, Y. Zhang, T. Wang, Cation-and pH-dependent hydrogen evolution and oxidation reaction kinetics, JACS Au 1 (2021) 1674–1687, https://doi.org/10.1021/jacsau.1c00281.
[44] M.C. Monteiro, F. Dattila, B. Hagedoorn, R. García-Muelas, N. López, M.T. Koper, Absence of CO_2 electroreduction on copper, gold and silver electrodes without metal cations in solution, Nat. Catal. 4 (2021) 654–662, https://doi.org/10.1038/s41929-021-00655-5.
[45] H.-G. Qin, F.-Z. Li, Y.-F. Du, L.-F. Yang, H. Wang, Y.-Y. Bai, M. Lin, J. Gu, Quantitative understanding of cation effects on the electrochemical reduction of CO_2 and H^+ in acidic solution, ACS Catal. 13 (2022) 916–926, https://doi.org/10.1021/acscatal.2c04875.
[46] Y.C. Li, G. Lee, T. Yuan, Y. Wang, D.-H. Nam, Z. Wang, F.P. García de Arquer, Y. Lum, C.-T. Dinh, O. Voznyy, CO_2 electroreduction from carbonate electrolyte, ACS Energy Lett. 4 (2019) 1427–1431, https://doi.org/10.1021/acsenergylett.9b00975.
[47] Z. Zhang, E.W. Lees, F. Habibzadeh, D.A. Salvatore, S. Ren, G.L. Simpson, D. G. Wheeler, A. Liu, C.P. Berlinguette, Porous metal electrodes enable efficient electrolysis of carbon capture solutions, Energy Environ. Sci. 15 (2022) 705–713, https://doi.org/10.1039/D1EE02608A.
[48] C.P. O'Brien, R.K. Miao, S. Liu, Y. Xu, G. Lee, A. Robb, J.E. Huang, K. Xie, K. Bertens, C.M. Gabardo, Single pass CO_2 conversion exceeding 85% in the electrosynthesis of multicarbon products via local CO_2 regeneration, ACS Energy Lett. 6 (2021) 2952–2959, https://doi.org/10.1021/acsenergylett.1c01122.
[49] IEA, Key World Energy Statistics 2020. ⟨https://www.iea.org/reports/key-world-energy-statistics-2020⟩, 2020.
[50] J. Lee, W. Lee, K.H. Ryu, J. Park, H. Lee, J.H. Lee, K.T. Park, Catholyte-free electroreduction of CO_2 for sustainable production of CO: concept, process development, techno-economic analysis, and CO_2 reduction assessment, Green. Chem. 23 (2021) 2397–2410, https://doi.org/10.1039/D0GC02969F.